Acta Materialia 207 (2021) 116654

Contents lists available at ScienceDirect

Acta Materialia

journal homepage: www.elsevier.com/locate/actamat

Effect of Si content on the uniaxial tensile behavior of Mo-Si solid solution alloys

Xiang Yu, Zhi Li, Padam Jain[1], Huajian Gao[2,3], Sharvan Kumar*

School of Engineering, Brown University, 184 Hope Street, Providence, RI 02912, United States

ARTICLE INFO

Article history:
Received 4 October 2020
Revised 18 December 2020
Accepted 13 January 2021
Available online 19 January 2021

Keywords:
Molybdenum solid solution
Yield strength
Ductility
Dynamic strain aging
Atomistic simulations

ABSTRACT

Recrystallized binary Mo-0.2 wt.% Si (Mo-0.68 at.% Si) and Mo-0.3 wt.% Si (Mo-1.0 at.% Si) alloys and a ternary Mo-0.75 wt.% Si-0.14 wt.% B (Mo-2.5 at.% Si-1.2 at.% B) alloy were tested in uniaxial tension as a function of temperature in vacuum and the results are compared to previous results on recrystallized commercial purity (CP) Mo and a binary Mo-0.1 wt.% Si (Mo-0.34 at.% Si) solid solution alloy. Yield strength increases with increasing Si content at all temperatures examined except at room temperature where the 0.1 wt.% Si alloy demonstrates softening; atomistic simulation confirms this behavior to be associated with Si segregation to the core and the associated ease of kink nucleation. Tensile ductility at room temperature rapidly deteriorates with increasing Si content in solid solution but in the Mo-0.3 wt.% Si solid solution alloy, tensile ductility of ~10% was measured at 300°C and thereafter, it increases rapidly at higher temperatures. Serrated flow occurs in the temperature range 600°C~800°C with the serration amplitude increasing with increasing Si content; atomistic simulation illustrates O trapping by Si in solid solution and subsequent de-trapping/release at higher temperatures that can account for the onset temperature delay of serrated flow in these Mo-Si solid solution alloys relative to commercial purity Mo. The serrated flow phenomenon is accompanied by significant work hardening; the presence of dislocation tangles, dipoles and prismatic loops in specimens fractured above $\geq$ 700°C accounts for the observed work hardening.

1. Introduction

For more than 70 years, aircraft engine propulsion has been a driver for understanding, designing and processing high-temperature structural materials. Such materials typically require a balance of high temperature strength, creep, and oxidation resistance and acceptable ambient temperature damage tolerance. Ni-base superalloys have been the material of choice for rotating structural components in the hot section of the engine but their melting temperature (~1400°C) limits their applications; advanced single-crystal airfoils that incorporate internal air-cooling passages and the use of thermal-barrier coatings have nevertheless enhanced their performance envelope [1–6]. Materials with higher melting temperatures are therefore being sought for elevated temperature applications in the aerospace industry beyond the capability of Ni-base superalloys. Refractory metals and alloys, intermetallics and ceramic matrix composites are all being examined as possible alternatives to nickel-based superalloys [7–11]. One family of alloys that has received research attention over the past two decades is the multiphase Mo-Si-B alloys composed of the Mo_5SiB_2 and Mo_3Si intermetallic phases embedded in a bcc-Mo solid solution matrix [7,12–18]. More recently, Mo-Si-B-TiC alloys [19,20] and Mo-Si-Ti eutectic and eutectoid alloys [21,22] are being explored as well to obtain a balance in toughness, creep and oxidation resistance within this family of alloys.

The mechanical properties of ternary multiphase Mo-Si-B alloys have been examined by various research groups at low and high temperatures [13,16,17,23–27]. These studies have shown that the Mo solid solution phase can limit creep behavior and dictate low temperature damage tolerance; furthermore, it has been shown that B solubility in the solid solution phase is negligible at low temperature and that it is the Si in solid solution that negatively influences the tensile ductility and fracture toughness of the phase [28]. Specifically, in powder-processed alloys that were HIPed and then annealed to grain sizes in the range of 30-100 μm, grain size dependence of ductility was marginal for the nominally pure Mo compact as well as a binary Mo-0.1wt.% Si compact. The frac-

* Corresponding author.
[1] Currently at Google Inc, 1600 Amphitheatre Pkwy, Mountain View, CA 94043, United States
[2] School of Mechanical and Aerospace Engineering, Nanyang Technological University, Singapore 639798, Singapore
[3] Institute of High Performance Computing, A*STAR, Singapore 138632, Singapore

https://doi.org/10.1016/j.actamat.2021.116654
1359-6454/

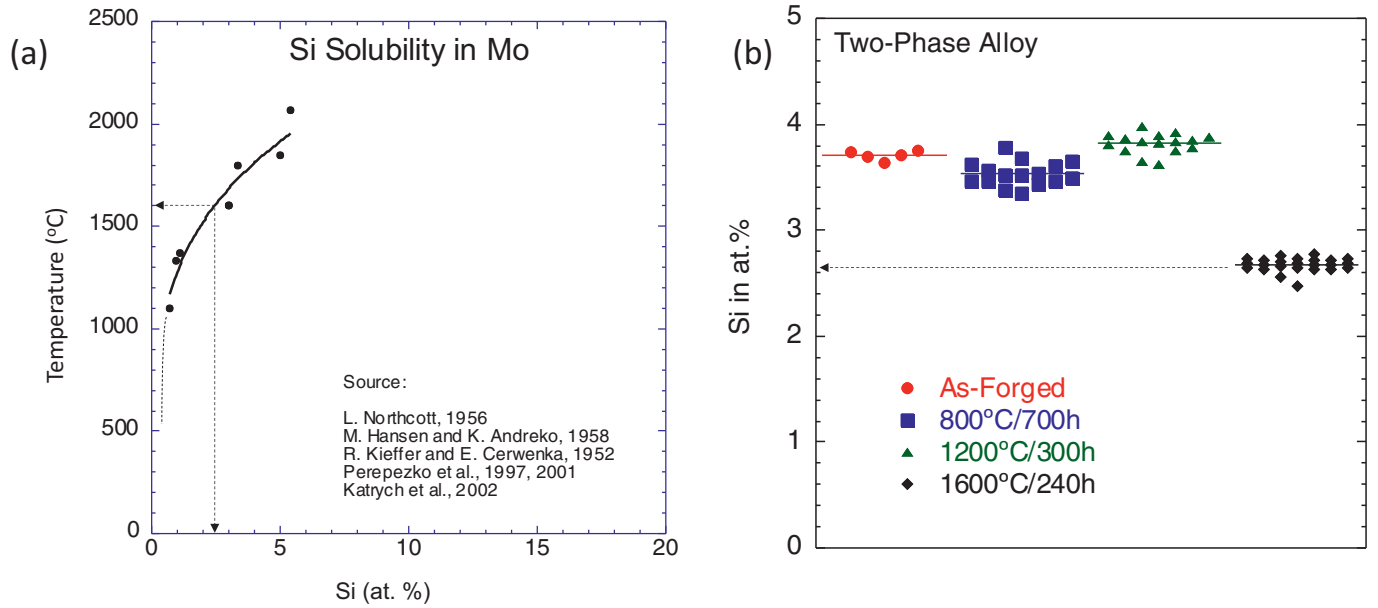

Fig. 1. (a) The effect of temperature on the solubility limit of Si in Mo from data in the literature [30–36]; (b) inability of extended anneals at 800°C and 1200°C to relieve matrix supersaturation of Si in Mo in a forged two-phase Mo-Si-B alloy composed of a supersaturated Mo-solid solution and the Mo_5SiB_2 phase [37] but enabled after 240h at 1600°C.

ture strain at room temperature for pure Mo was reported as 13% whereas for the Mo-0.1wt.%Si, the corresponding number was 0%, but was more than 20% at 260°C. More recently, the tensile response of recrystallized pure Mo sheet and of as-extruded and annealed ingot-metallurgy processed Mo-0.1 wt.% Si was reported at room and elevated temperatures [29]. In this latter study, as in the previous work of Sturm et al [28], solid solution softening was reported for the annealed Mo-0.1wt.%Si at room temperature, but in the as-extruded state as well as in the annealed state, contrary to the previous report, tensile ductility was reported at room temperature in the Mo-0.1 wt.%Si alloy (~10% in the as-extruded state and >50% in the annealed state). Reasons for this large discrepancy between these two reports are not clear and warrant further studies.

Sturm et al [28] also examined two other alloys with higher Si content (Mo-0.5 wt.%Si and Mo-1.0 wt.% Si) and reported a significant increase in yield strength at room temperature with increasing Si content and a *steep rise in* the brittle-to-ductile transition temperature as measured in terms of tensile fracture strain (a fracture strain of 3.3% was reported at 816°C for the Mo-0.5 wt.%Si alloy). It is worth noting that 0.5 wt.% Si and 1.0 wt.% Si translate into 1.69 at.% Si and 3.34 at.% Si, and these may well be above the solubility limit of Si in Mo at temperatures below 1200°C, the supersaturation resulting from the high processing temperatures adopted in that study (sintering at 1850°C, HIPing at 1500°C and hydrogen annealing in the range 1800°C-2000°C). Thus, it is not clear how alloys containing Si levels higher than 0.1 wt.% but less than the solubility limit will respond. Further, it is surprising that a small transition in Si content from 0.1 wt.%Si to 0.5 wt.%Si produces such a dramatic change in the ductile to brittle transition temperature.

The solubility of Si in Mo has been examined by various investigators and data from these investigations [30–36] have been compiled in Fig. 1a as a function of temperature. These data suggest that below 1200°C, Si solubility in Mo is ~1 at.% (~0.3 wt.%) or less. Furthermore, Jain and Kumar [37] reported on the supersaturation of Si in the Mo solid solution phase in a two-phase Mo-Si-B alloy resulting from high temperature processing, and the inability to relieve the supersaturation after extended anneals (800°C for 700h and 300h at 1200°C), reflecting the extremely sluggish kinetics. However, a higher temperature anneal at 1600°C for 240h (Fig. 1b) reduced the supersaturation to a value of ~2.5 at.% Si, commensurate with the solubility curve depicted in Fig. 1a and emphasizing the difficulty in eliminating supersaturation.

Thus, in order to understand the influence of Si in solid solution in Mo on the mechanical properties of the solid solution phase, it would be instructive to examine binary alloys where the Si content in Mo lies below 0.3 wt.% Si (1 at.% Si); furthermore, it would also help to rationalize why there is so much of a difference in the response recorded for the Mo-0.1 wt.% Si alloy in the two studies [28,29] described above. This study addresses these issues through a combination of experiments and simulations focusing on the mechanical behavior of three alloys containing 0.2 wt.% Si (0. 68 at.% Si), 0.3 wt.% Si (1.0 at.% Si) and a ternary alloy, Mo-0.75 wt.% Si-0.14 wt.% B (Mo-2.5 at.% Si-1.2 at.% B) in the recrystallized condition. The ternary alloy is supersaturated in Si and includes some relatively coarse second-phase particles but serves to illustrate a trend in properties. It is noted that the Si level in this ternary alloy lies between the values of 0.5 wt.% Si and 1.0 wt.%Si mentioned above from the work of Sturm et al [28].

2. Experimental procedure

Extrusions of Mo-Si solid solution alloys with compositions of Mo-0.2 wt.% Si and Mo-0.3 wt.% Si were produced at Pittsburgh Materials Technology Inc. in Pittsburgh, PA (USA) as described below. High purity powders of Mo, Si, and B were blended and first arc-melted in a trough to produce an electrode in each instance. An ingot of each alloy was then produced by double vacuum arc remelting with dimensions of ~5 cm diameter and 15 cm length. The ingots were sealed in Molybdenum cans and induction-heated to 1550°C in an argon atmosphere, soaked for 10 minutes at temperature and then hot-extruded using a high velocity Dynapak extrusion press using a 4:1 reduction ratio. The usable portion of the resulting extrusions was approximately 30 cm long. Wet chemical analysis showed the carbon and oxygen levels in the Mo-0.2 wt.% Si to be 0.005-0.006 wt.% and 0.002-0.003 wt.% respectively, while the corresponding values were 0.003 wt.% and 0.002 wt.% in the Mo-0.3 wt.% Si alloy.

In addition, a third alloy with a target composition of Mo-0.9 wt.%Si-0.15 wt.%B that was produced at an earlier time, also at Pittsburgh Materials Technology Inc. in Pittsburgh, PA (USA), using parameters similar to those described above, was included in this study. Chemical analysis of this extrusion yielded a composition of Mo-0.75 wt.%Si-0.14 wt.%B and C and O concentrations of 0.001 wt.% and 0.002 wt.%, respectively. The marginally two-phase extruded microstructure was composed of a supersaturated Mo solid solution and ~5 vol.% of relatively coarse, second-phase particles. The extruded microstructure was fully recrystallized with a grain size of ~20 μm and mechanical properties were obtained in this state.

As-received samples for optical microscopy were electro-discharge machined (EDM) and were mounted in conductive copper-impregnated thermoset, ground using standard 240, 400, 600, and 800 grit abrasive discs and polished using 1 µm diamond solution. The polished surface was electrolytically etched using a solution of 10 g oxalic acid dissolved in 100 ml of distilled water at 5 V for 1~2 s to reveal grain boundaries. The microstructures were examined using an optical microscope and a LEO 1530VP scanning electron microscope (SEM). Thin foils of Mo-Si solid solution alloys for transmission electron microscope (TEM) observations were made from slices, which were ground to a thickness of 60~100 µm. Disks, 3 mm in diameter, were mechanically punched out of these thin slices. Final thinning and perforation of the foils were accomplished by a Tenupol twin-jet electropolisher using a solution of 125 mL sulfuric acid in 875 mL methanol at ~ -30°C and using 20 V. The samples were examined in a CM20 TEM operating at 200 kV.

Uniaxial tensile tests were performed using flat, dog-bone shaped specimens with a gauge length of ~20 mm, a gauge width of 1.8 mm, and thickness of 2 mm. These were electro-discharge machined along the extrusion axis. Both flat surfaces of the tensile specimens were ground and polished. The tensile tests on Mo-Si solid solution alloys were performed in the temperature range of 20°C to 1000°C at a nominal strain rate of 5×10^{-4}/s. The Mo-Si-B solid solution alloy was tested in the temperature range of 400°C~1200°C at a nominal strain rate of 10^{-4}/s; a few tests were also conducted at 10^{-6}/s. Room-temperature tests were conducted in air whereas at higher temperatures, a Centorr furnace equipped with tungsten mesh heating elements and a diffusion pump capable of generating a vacuum of ~1.33×10^{-3} Pa at the test temperatures was used. A tungsten-rhenium thermocouple was used to measure the temperature in the furnace. All the tensile tests were performed using grips machined from a TZM alloy. Tensile tests were conducted generally in duplicate for the solid solution alloys and all tests were taken to fracture. Deformed microstructure was characterized by TEM using the approach described previously to produce the electron-transparent specimens.

3. Experimental results

3.1. Microstructure

Representative optical micrographs for the *as-extruded* Mo-0.3wt.%Si and Mo-0.2wt.%Si alloys are shown in Fig. 2a,b. The average grain size of the Mo-0.3wt.%Si alloy is ~80 µm (Fig. 2a). In contrast, the average grain size of the Mo-0.2wt.%Si alloy appears to be around 10 µm (Fig. 2b) and in both alloys, the grains are fairly equiaxed. It is somewhat surprising that the grain size in the as-extruded material is finer in the more dilute alloy (as one might expect more effective solute drag on grain boundaries inhibiting grain growth) but as the processing was performed at Pittsburgh Materials Technology Inc. we did not have direct oversight over the processing parameters utilized including extrusion temperature and strain rates.

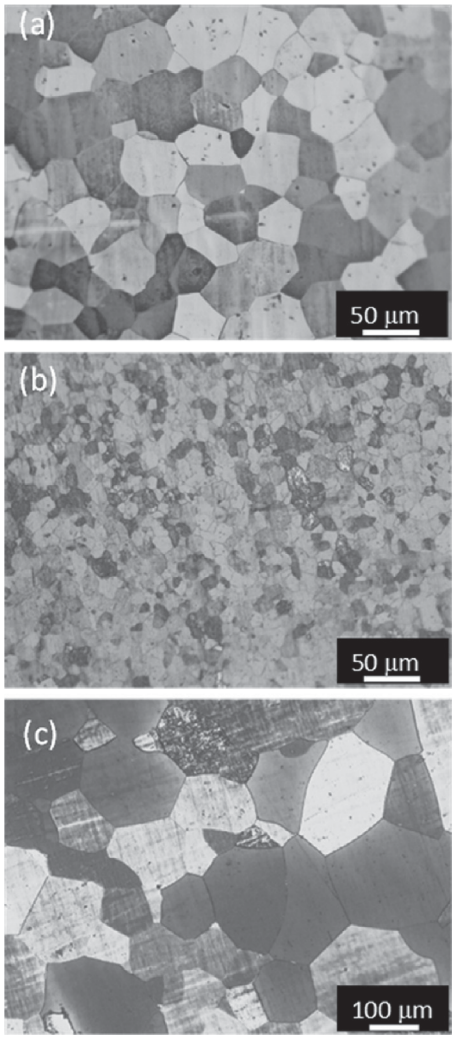

Fig. 2. Initial microstructure: (a) as-extruded Mo-0.3wt.%Si alloy, (b) as-extruded Mo-0.2wt.%Si alloy, and (c) annealed (1600°C/4h) Mo-0.2wt.%Si alloy.

Heat treatments at 1400°C, 1500°C and 1600°C for 4 h were conducted on the Mo-0.2wt.%Si alloy to grow the grains to a size similar to that of the Mo-0.3wt.%Si alloy and this was achieved for the 1600°C/4h treatment (Fig. 2c). Electron Backscatter Diffraction (EBSD) images for both solid solution alloys confirmed random texture. Optical microscopy examination of the as-extruded Mo-0.75 wt.% Si-0.14 wt.% B alloy also confirmed a fully recrystallized microstructure with equiaxed grains of size ~20 µm (Fig. 3). The dark particles in Fig. 3 were identified as T_2 particles based on SEM-EDX analysis of the Mo-to-Si ratio (Mo_5SiB_2) as B is not detected; their volume fraction was low (~5 vol.%) and these coarse particles were aligned in the extrusion direction. Transmission electron microscope (TEM) examination showed a low dislocation density in the annealed Mo-0.2wt.%Si, as well as in the as-extruded Mo-0.3wt.%Si, and Mo-0.75 wt.%Si-0.14 wt.%B alloys (Fig. 4a-c), and thus, the contribution from previous work hardening resulting from the extrusion process can be excluded.

3.2. Tensile behavior

The tensile stress-strain curves for the annealed Mo-0.2wt.%Si alloy obtained at different temperatures and at a nominal strain rate of 5×10^{-4}/s are shown in Fig. 5a. At room temperature, a distinct yield point of ~340 MPa was observed. The curve had a very short stress plateau immediately after yielding followed by signif-

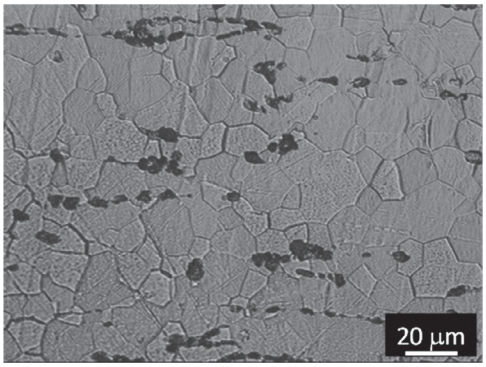

Fig. 3. As-extruded microstructure of the Mo-0.75 wt.%Si-0.14 wt.%B "solid solution" alloy. The dark particles strung out in the extrusion direction (horizontal) were identified as T2 (Mo_5SiB_2) particles.

icant work-hardening and a fracture strain of ~5%. At 300°C, the yield strength was lowered by about 40% and a stress plateau immediately after yielding is barely visible. The work-hardening rate was still high, doubling in strength to a maximum prior to failure and accompanied by a plastic strain to failure of about 20%. At 700°C, both the yield strength and the work-hardening rate were reduced and a stress plateau was not evident; however, serrated flow is noted (as also at 800°C) and is accompanied by a visible loss in ductility relative to that observed in the 500°C specimen. At 1000°C, there was no distinct yield point and work-hardening was negligible; the fracture strain at 1000°C was ~34%.

The tensile stress-strain curves for the Mo-0.3wt.%Si alloy are provided in Fig. 5b. At room temperature, the material exhibits a high yield strength (~390 MPa) and negligible plastic strain (~0.1-0.2%) and therefore there is not an opportunity to discern a stress plateau beyond yielding. At 300°C, the yield strength is lower, the fracture strain increases to ~20%, and there is a short but clearly visible stress plateau before conventional work hardening commences. At 500°C, 700°C and 800°C, the yield strength is further lowered relative to 300°C and the stress plateau persists, although progressively less evident. The ductility increases to ~35% at 500°C. At 700°C and 800°C, serrated flow is observed and the work-hardening rate is comparable to the 300°C specimen; the fracture strain decreases to about 28%. Compared with the curve at 500°C, the 700°C and 800°C specimens show higher work hardening rates and flow stresses and a relative loss in ductility. At 1000°C, there is no distinct yield point, the fracture strain is about 42%, and work-softening is noted, although early in the plastic deformation regime, work-hardening is observed. Such a transition to work softening is usually related to thermally activated softening processes (such as dynamic recovery and/or recrystallization); in this case, evidence is presented for dynamic recovery in Fig. 8e in Section 3.3.

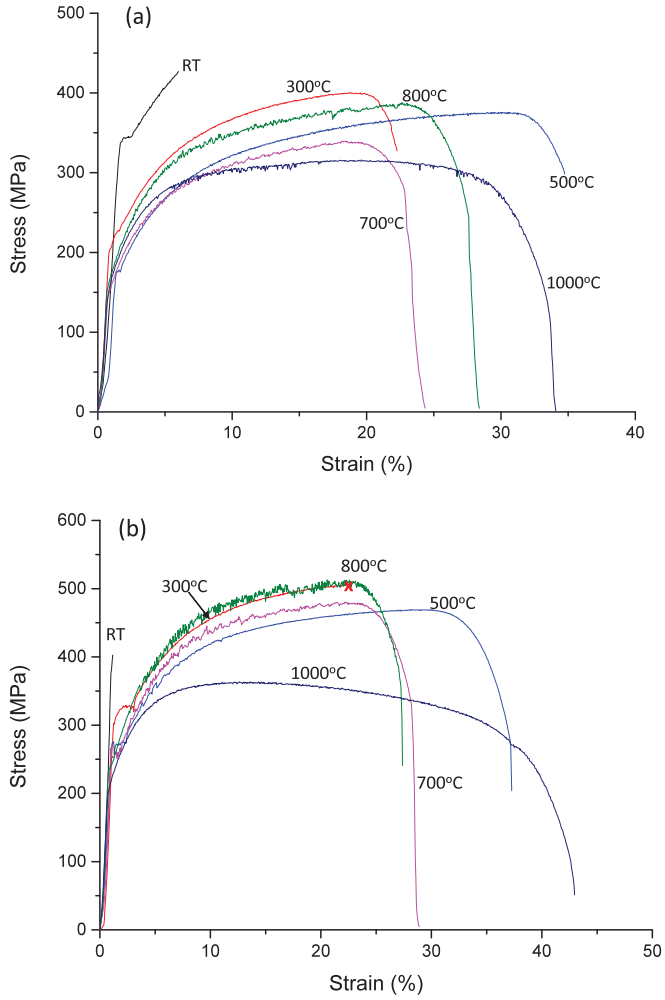

Fig. 5. The uniaxial tensile stress-strain curves at a nominal strain rate of 5×10^{-4}/s for various temperatures for (a) the annealed Mo-0.2wt.%Si alloy, and (b) the Mo-0.3wt.%Si alloy. In (b), the 'x' denotes fracture of the 300°C specimen.

The plastic portion of the tensile stress-strain curves for the Mo-0.75 wt.%Si-0.14 wt.%B alloy in the temperature range 400°C-1200°C, generated at a nominal strain rate of 1.0×10^{-4}/s are presented in Fig. 6a, b and d. In addition, the effect of testing at a slower strain rate of 10^{-6}/s on the tensile response at 700°C is compared in Fig. 6c. At and below 400°C, the specimens failed in a brittle manner and so only the fracture stress at 400°C (~730 MPa) is included in Fig. 6a.

Upper yield points of 560 MPa and 500 MPa followed by a significant drop in stress to corresponding lower yield points of 440 MPa and 400 MPa are noted at 500°C and 600°C respectively. Im-

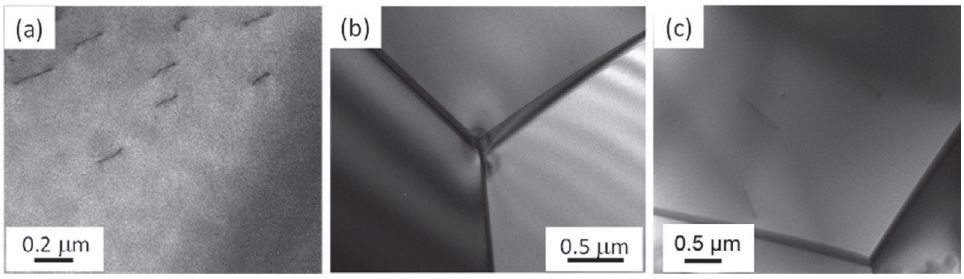

Fig. 4. Representative TEM micrographs illustrate low dislocation densities in the three alloys examined: (a) Mo-0.2wt.%Si, (b) Mo-0.3wt.%Si, and (c) Mo-0.75 wt.%Si-0.14 wt.%B.

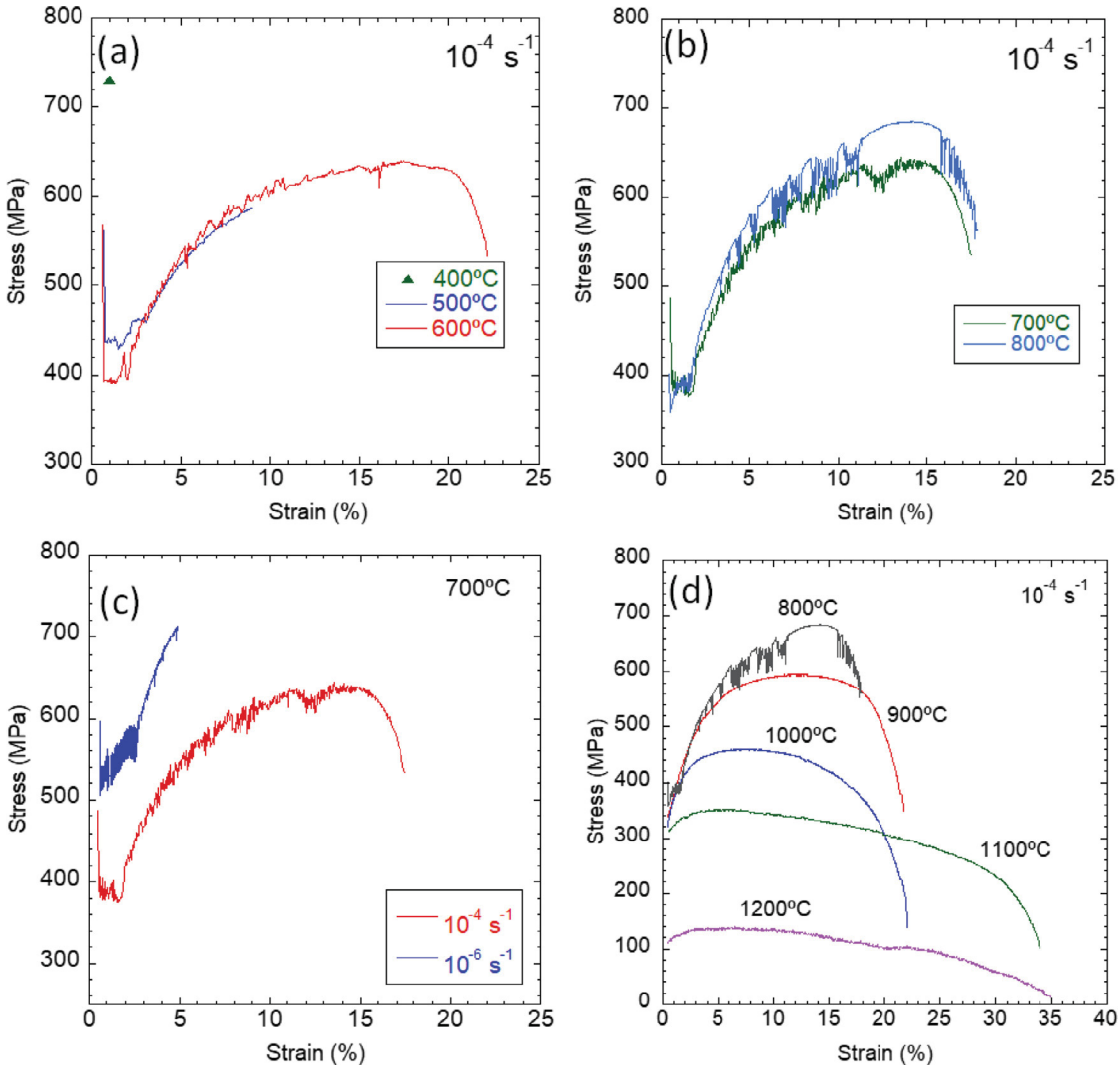

Fig. 6. The plastic portion of the uniaxial tensile stress-strain curves for the ternary Mo-0.75 wt.%Si-0.14 wt.%B alloy: (a) 400°C-600°C (10^{-4}/s), (b) 700°C and 800°C (10^{-4}/s), (c) 700°C at 10^{-4}/s and 10^{-6}/s, and (d) 800°C-1200°C (10^{-4}/s). The 800°C curve is repeated in (d) as a baseline to illustrate the absence of pronounced serrations at 900°C and higher.

mediately after the lower yield points, distinct yield plateaus are observed, following which work hardening commences. At 600°C, the flow curve illustrates serrated flow. A similar response is observed in Fig. 6b at 700°C and 800°C with a plateau stress around 390 MPa followed by work-hardening. Serrated flow is also evident at these temperatures and a loss in failure strain (~17%) relative to that observed at 600°C (~22%) in Fig. 6a is observed. At the reduced strain rate of 10^{-6}/s at 700°C, serrated flow is more pronounced and is accompanied by an increased strength, increased work-hardening rate and reduced strain to fracture (Fig. 6c). At slower strain rates within the dynamic strain aging (DSA) regime, opportunities present themselves for solute to effectively segregate to forest dislocations and to transfer to mobile dislocations during "waiting times" at obstacles, producing an increase in work-hardening and a loss in elongation to failure [38–41].

At higher temperatures, the yield stress drops (~320 MPa at 1000°C, ~300 MPa at 1100°C and to ~100 MPa at 1200°C), the yield plateau disappears, and the flow curves are not serrated (Fig. 6d). There is a corresponding increase in fracture strain from about 23% at 900°C to ~35% at 1200°C. In short, the early stage plastic deformation instabilities observed (such as a stress plateau and serrated flow) in the dilute alloys (0.2 wt.% Si and 0.3 wt.% Si) are exaggerated in this higher Si-containing alloy in the same temperature range.

The variations in yield strength and tensile ductility for these three alloys (Mo-0.2 wt.%Si, Mo-0.3 wt.%Si and Mo-0.75 wt.%Si-0.14 wt.%B) together with data for annealed commercial purity (CP) Mo and a Mo-0.1 wt.%Si alloy annealed at 1600°C for 4h, both from a previous study [29] are presented in Fig. 7a and b respectively. Data for the annealed Mo-0.1 wt.%Si alloy were only available at room temperature, 300°C and 700°C. At room temperature, the Mo-0.1 wt.%Si alloy is softer than CP Mo and this was also previously noted by Sturm et al [28]. This effect is not observed at elevated temperatures. Also, the softening effect is not observed for higher Si levels at room temperature. For all other temperatures examined and up to 1000°C, the yield strength at any given temperature increases with increasing Si content. At 1200°C, the strength drops precipitously for the ternary Mo-0.75 wt.%Si-0.14 wt.%B alloy. Both CP Mo and the binary Mo-0.1 wt.%Si alloy retain good ductility at room temperature. However, for higher Si content, tensile ductility drops rapidly and is ~4 percent for the Mo-0.2 wt.%Si at room temperature, while the Mo-0.3 wt.%Si and the ternary Mo-0.75 wt.%Si-0.14 wt.%B alloys failed in a brittle manner. At 300°C, both, the Mo-0.2 wt.%Si alloy and the Mo-0.3 wt.%Si

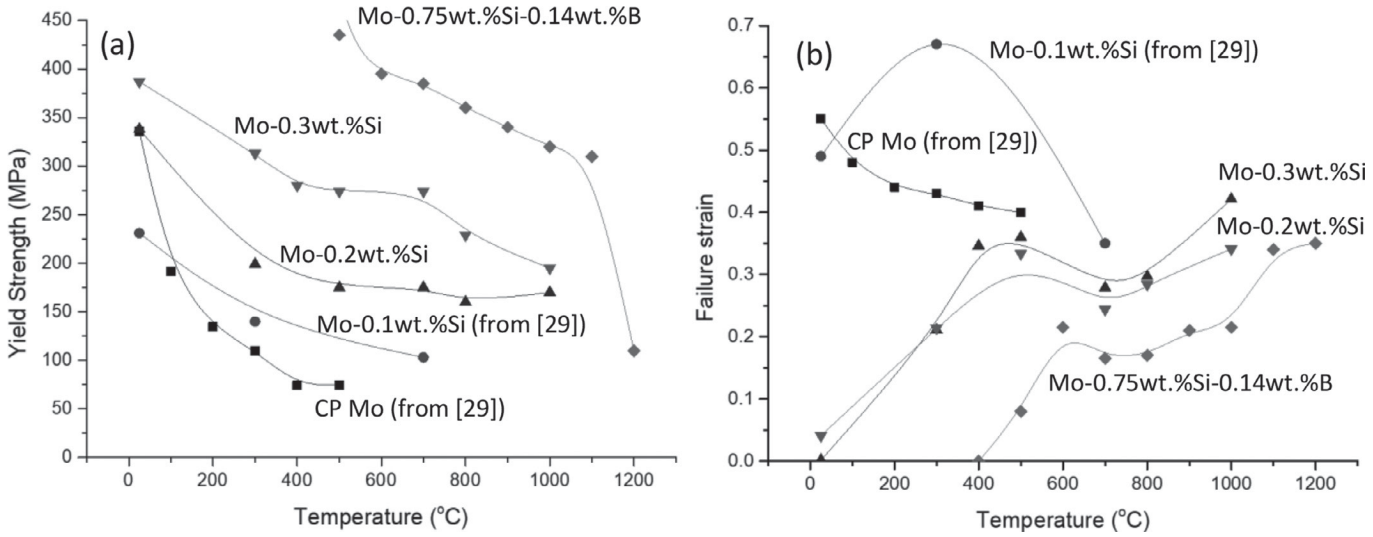

Fig. 7. The effect of temperature on (a) yield strength and (b) tensile elongation for commercial purity (CP) Mo, binary Mo-0.1 wt.%Si, Mo-0.2 wt.%Si, Mo-0.3 wt.%Si and ternary Mo-0.75 wt.%Si-0.14 wt.%B alloys. The data for CP Mo and Mo-0.1 wt.%Si were obtained from [29].

alloy exhibited significant plastic strain to failure (~20%). In contrast, the ternary alloy continued to fail in a brittle manner at this temperature and only demonstrated ductile failure at 500°C with a tensile elongation of ~7-8 percent. All three alloys examined in this study showed further increases in ductility at 600°C before showing some loss in ductility at 700°C and 800°C coincident with serrated flow (This ductility loss is also seen in the Mo-0.1 wt.%Si alloy by comparing the failure strain at 300°C with that at 700°C in Fig. 7b, consistent with serrated flow at the latter temperature reported in [29]). Beyond 800°C, ductility increased once again with increasing temperature. It is evident that increasing the Si content in solid solution in the alloy progressively decreases ductility at a given temperature and increases the brittle-to-ductile transition temperature. However, it is also worth noting that when the Si content is 0.3 wt.% (around the solubility limit below 1200°C), the ductility is ~20 percent at 300°C and does not drop below that value for all higher temperatures examined.

3.3. Deformed microstructure

The post-deformed microstructures in the Mo-0.2 wt.%Si, Mo-0.3 wt.%Si alloys and in the Mo-0.75 wt.%Si-0.14 wt.%B alloy were examined by TEM to develop an appreciation for the effect of composition, temperature and strain on the dislocation structure evolution in these solid solution alloys. These three alloys displayed several similar characteristics, with total strain accumulated and test temperature being the primary factors that influenced the evolving dislocation arrangements. Thus, to keep redundancy to a minimum, representative bright field images were selected from these three alloys examined at different temperatures and strain rates and these are presented in Fig. 8a-f to illustrate some of these aspects.

Fig. 8a displays the dislocation configuration in a Mo-0.2wt.% Si tensile specimen taken to fracture at the strain rate of 5×10^{-4}/s at room temperature. A defined cell structure had not fully developed after ~4% plastic strain; instead, loose dislocation tangles were present amidst dislocation-free areas. At a higher test temperature of 500°C, the fracture strain at the same strain rate for the Mo-0.3 wt.%Si specimen was ~36% and the microstructure in the foil mostly consisted of well-defined cell walls composed of dense dislocation tangles; the cell size was ~0.7 μm and the cell interiors were fairly dislocation-free (Fig. 8b). A similar microstructure was also observed in the Mo-0.2 wt.%Si alloy after a comparable strain at this temperature.

The Mo-0.75 wt.%Si-0.14 wt.%B specimen tested at 700°C/10^{-6} s^{-1} (Fig. 8 c,d) was one that fell within the DSA regime and exhibited pronounced DSA effects (Fig. 6c) and a fracture strain of ~4-5%. In this specimen, a dislocation cell structure is not present but a significant level of pinning and bowing of dislocations is evident. It is noted that these pinning points are free of any precipitate, implying that pinning is either due to solute atom clusters or unit/superjogs. A large number of dislocation dipoles were observed and confirmed through **±g** analysis (white dashed circle in Fig. 8 c,d is one example). In the **±g** analysis, a change in the distance between the parallel segments of the dislocations on reversing the **g** vector verifies the presence of a dislocation dipole.

When the test temperature was increased to 1000°C, at the nominal strain rate of 10^{-4} s^{-1}, the strain to failure increased (>20% for the ternary alloy and >30% for the 0.2 wt.%Si and 0.3 wt.%Si alloys), and in general, well-developed subgrains were observed, indicative of dynamic recovery; an example is shown in Fig. 8e for the Mo-0.3 wt.%Si alloy that experienced ~40% fracture strain. In addition, in these solid solution alloys, dislocation loops 50 to 120 nm in diameter were observed in the specimens deformed in the temperature range 700°C-1000°C. An example of these is illustrated in Fig. 8f corresponding to the Mo-0.2wt.%Si alloy deformed at 1000°C at a strain rate of 5×10^{-4}/s and after experiencing 33% plastic strain to failure.

A diffraction analysis was performed to understand the character of these dislocation loops. A reference two-beam bright field image of such loops in a deformed Mo-0.75 wt.%Si-0.14 wt.%B specimen (1000°C, 10^{-4} s^{-1}) and obtained using **g** = [200] is shown in Fig. 9a (labeled 1, 4 and 5). A **g.b** analysis was performed using additional **g** vectors (Fig. 9b-e) that provided invisibility conditions (Fig. 9b-d) to verify that the loops marked 1, 4 and 5 in Fig 9a have a Burgers vector of ½ [$\bar{1}$11]. The specimen was tilted until the plane containing loop 1 was almost vertical and was imaged in a two-beam condition using the **g** vector $\bar{1}$11. As seen, the **g** vector is perpendicular to the loop suggesting the loop lies on the ($\bar{1}$11). This implies that the Burgers vector of loop 1 is perpendicular to the plane on which it lies, and therefore it is a prismatic loop. Dislocation 2 has a Burgers vector of ½ [111], while for dislocation 3, it is ½ [1$\bar{1}$1].

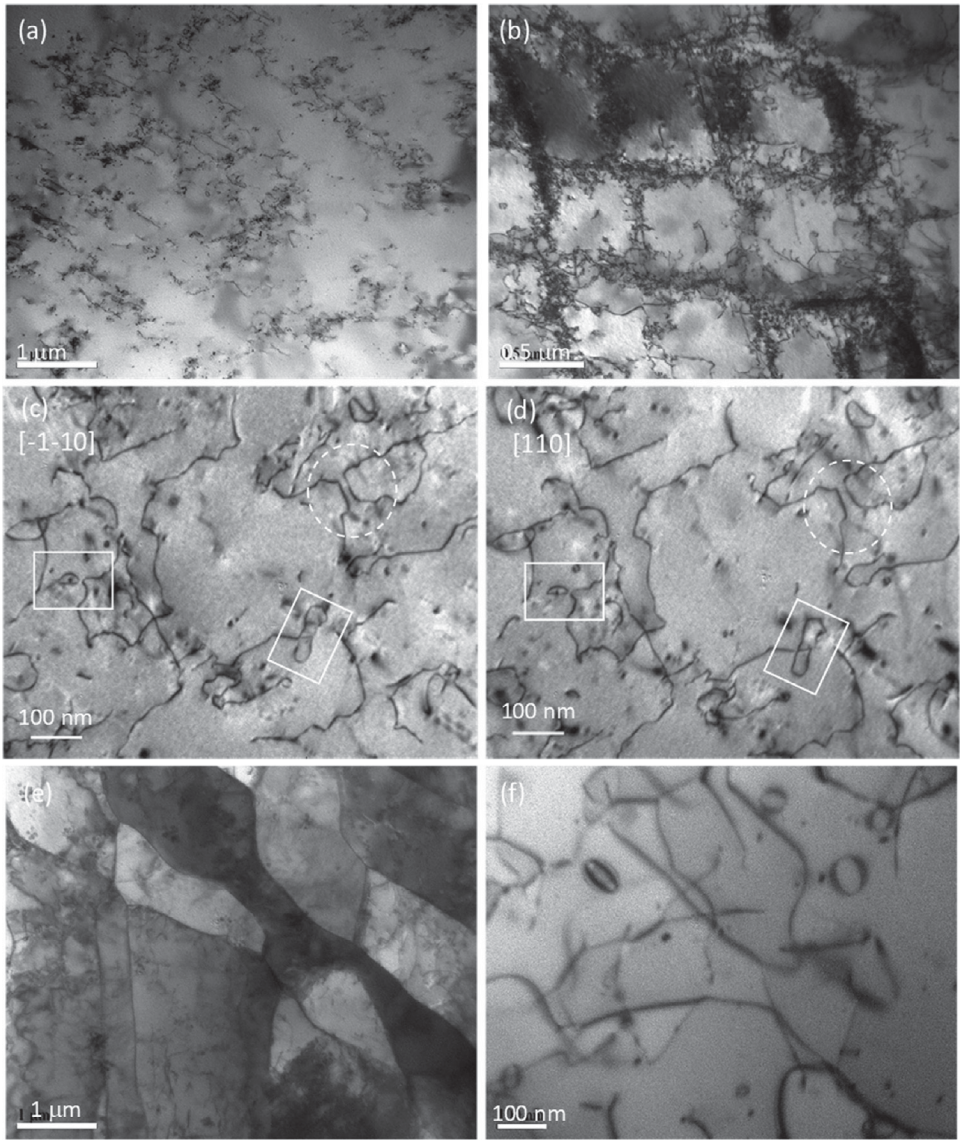

Fig. 8. (a) Annealed Mo-0.2wt.%Si deformed at the strain rate of 5×10^{-4}/s at room temperature (4% strain), (b) Mo-0.3wt.%Si deformed at 500°C/5×10^{-4}/s (36% strain), (c,d) 700°C/10^{-6} s^{-1} (**±g** analysis) to confirm the presence of dislocation dipoles (dashed circle) in Mo-0.75 wt.% Si-0.14 wt.% B, (e) Mo-0.3wt.%Si deformed at 1000°C/5×10^{-4}/s (40% strain) and (f) Mo-0.2wt.%Si deformed at 1000°C/5×10^{-4}/s (33% strain). Regions enclosed by the white rectangles show an elongated dislocation loop and an elliptical loop that appears to have pinched off from a dislocation segment.

4. Simulation method

We performed first principle denisty functional theory (DFT) calculations using the Vienna ab initio simulation package (VASP). These calculations used projector augmented wave method (PAW) [42,43] with the Perdew-Burke-Ernzerhof (PBE) Generalized Gradient Approximation (GGA) [44] for exchange-correlation. The PAW potential adopted in this work explicitly treats 14, 4 and 6 valence electrons respectively for Mo, Si and O atoms. A plain wave cut-off energy of 400 eV was used in all calculations. The 270 atoms supercell containing a screw dislocation dipole with a length of 2*b*, where *b* is the Burgers vector length in the 1/2[1 1 1] direction as shown in Fig. 10a, is used to calculate the dislocation core structure in Mo-Si alloys. The atoms positions are initially deformed according to the displacement field of screw dislocations calculated using anisotropic elasticity [45] and subsequently fully relaxed with conjugate gradient algorithm until the forces are less than 1 meV/Å. Brillouin zone integrations were performed by using a Monkhorst–Pack scheme with $1 \times 2 \times 8$ k-points mesh, where the third direction is along the dislocation line. Similar set up has been widely used to calculate the dislocation core structure in BCC metals [46,47]. The 128 atoms bulk supercell as shown in Fig. 12a is adopted to calculate the Si and O aggregation in bulk Mo and a $4 \times 4 \times 4$ k-points mesh is used to provide sufficient convergence for the energy calculations. A substitutional Si atom is introduced to the bulk Mo supercell and interstitial O atoms are inserted around the Si atom. All atom positions are fully relaxed with conjugate gradient algorithm until the forces are less than 1 meV/Å.

5. Simulation results

5.1. Dislocation core structure

The differential displacement map in Fig. 10a shows the screw dislocation core structure in pure Mo. The calculated easy core structure with three-fold symmetry is consistent with previous calculations [46,48]. In Mo-Si alloys, Si atoms are believed to occupy

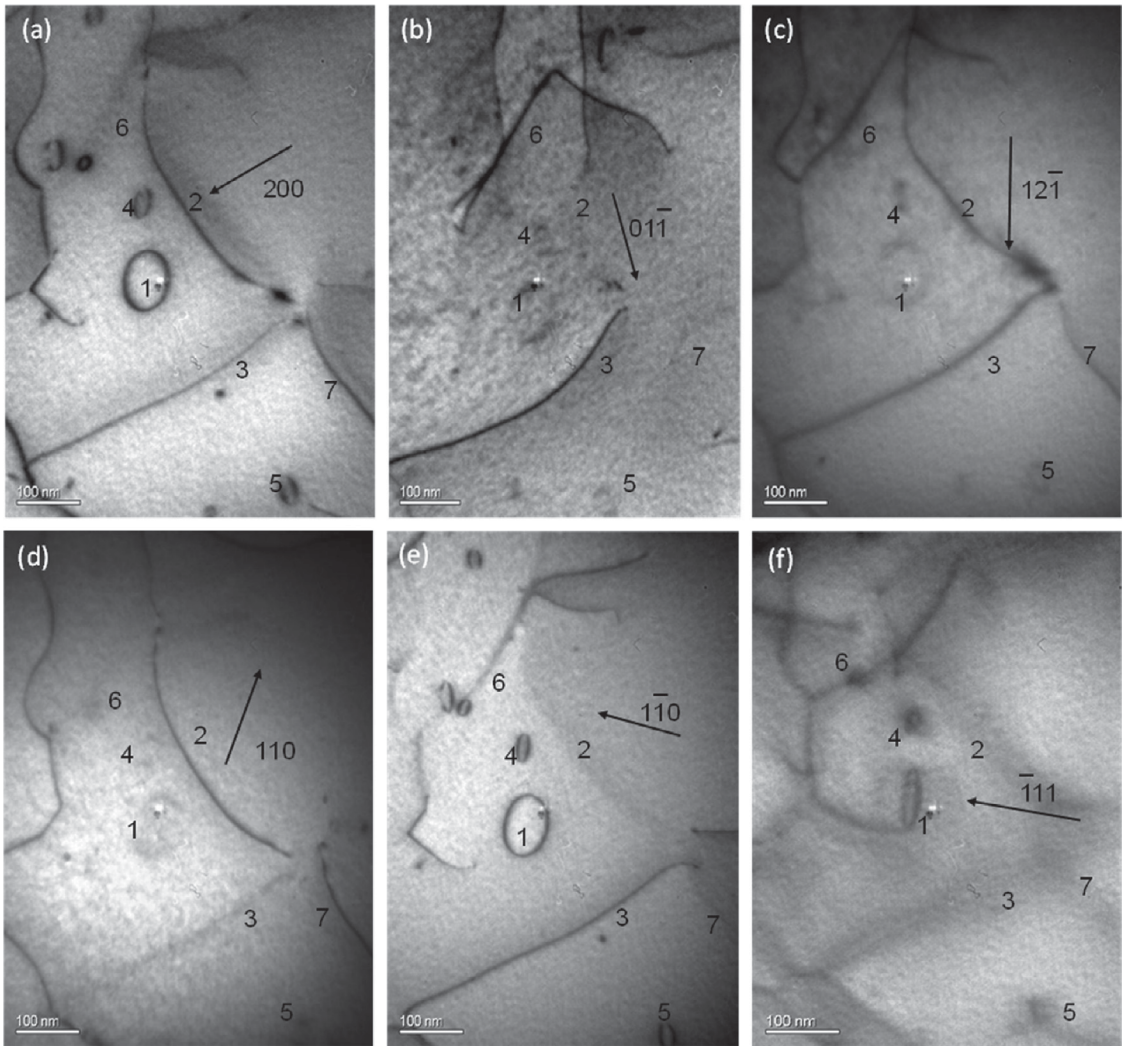

Fig. 9. Dislocation loops in the 1000°C/10^{-4} s^{-1} deformed Mo-0.75 wt.%Si-0.14 wt.%B specimen: (a) dislocation loops show sharp contrast for $\boldsymbol{g} = 200$, whereas they are invisible in (b-d) for $\boldsymbol{g} = 01\bar{1}$, $\boldsymbol{g} = 12\bar{1}$, and $\boldsymbol{g} = 110$. In (e), the loops are visible, but dislocation marked 2 is invisible as well as in (b). In (f), loop 1 is titled edge-on and the **g** vector $\bar{1}11$ is perpendicular to the plane of the loop.

only the substitutional sites due to their similar atomic radius to Mo atoms. To study the effects of Si on dislocation core structure, a substitutional Si atom is subsequently inserted into the supercell and separated from its image atoms along the Z direction by 2*b* to avoid strong solute-solute interactions. It is found that the most energetically favorable configuration is the one where the inserted Si atom stays at the dislocation core center as shown in Fig. 10b. The solute-dislocation interaction energy is defined as the energy difference between the configurations that Si is in and when it is infinitely separated from the dislocation core and is calculated as -0.56 eV, indicating strong attraction between substitutional Si atoms and screw dislocation cores. The solute-dislocation interaction energy decreases to -0.05 eV as the inserted Si atom moves 5.4 Å away from the core center (4^{th} nearest neighbor in (1 1 1) plane). This supports the previous experimental observation of Si segregation to dislocation cores in Mo-Si alloys [24]. The differential displacement map in Fig. 10b shows the same three-fold easy core structure as the pure Mo case, suggesting that no substantial change in core structure is associated with Si solute atoms being present in the core.

Oxygen is often present in Mo in hundreds of ppm, and while the majority is thought to segregate to grain boundaries [49,50], some part of it can remain as interstitial solid solution in the matrix and influence flow behavior. Interplay between interstitial O atoms and the screw dislocation core in Mo was next examined by inserting an oxygen atom in the nearest interstitial sites at the dislocation core. This causes the original compact easy-core structure to change to a new hard-core structure after relaxation as shown in Fig. 10c. This solute-induced core structure change has been reported in other BCC materials and is attributed to the large Voronoi volume of the interstitial prism site inside the hard core [51]. The oxygen-dislocation core interaction energy in Mo is calculated as -1.66 eV, suggesting strong attraction between O atoms and screw dislocations. This interaction energy in Mo is similar to the oxygen-dislocation interaction energy reported in the W-O system calculated from DFT where the interaction was examined in the context of serrated flow occurring when the solute and dislocation had comparable mobilities [52].

5.2. Solute softening and hardening

Solute-induced softening and hardening in Mo have been previously discussed within the context of thermally activated motion of dislocations by double-kink nucleation and kink migration [53]. The strong and relatively long-range attraction between Si and the screw dislocation core noted in this study can modify the

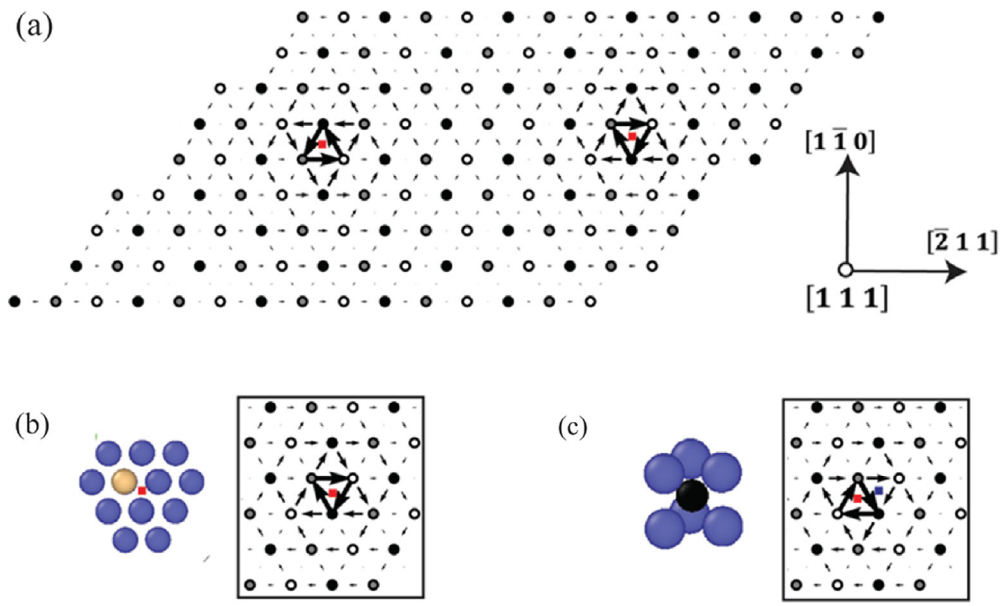

Fig. 10. (a) screw dislocation dipole model and differential displacement map for equilibrated pure BCC molybdenum. The red dots represent the location of dislocation cores. (b) Close-up view of the equilibrated easy core structure after Si substitution. (c) Close-up view of the equilibrated hard-core structure with interstitial oxygen. The blue dot represents the location of the center of original easy core. The red dot represents the center of the equilibrated hard core. Mo, Si and O atoms are blue, orange, and black.

energy scale of kink nucleation and lead to solute softening at low Si concentration as reported previously in the Mo-0.1 wt.%Si alloy at room temperature [28,29]. For higher Si solute concentration or higher temperature, kink migration could become the rate-limiting process and outweigh the softening effects from double kink nucleation, resulting in solute hardening in the Mo-Si alloys.

To determine if this is indeed the case, we have implemented a solid solution model for Mo-Si alloys where the applied stress σ is related to the strain rate $\dot{\epsilon}$ through the Orowan equation [53],

$$\dot{\epsilon} = 0.94b^2\rho\left(\Omega_n^{-1} + \Omega_m^{-1}\right)^{-1} \quad (1)$$

where b is the length of burger vector, ρ is the mobile dislocation density which is set at 10^8 cm^{-2} in the model, Ω_n is the double kink nucleation rate and Ω_m is the kink migration rate. Ω_n and Ω_m are expressed as functions of applied stress σ and solute concentration c,

$$\Omega_n = \nu_{dk} exp\left(-\frac{\Delta H_{dk}(\sigma, c)}{k_B T}\right)\left((1-c) + c \cdot exp\left(-\frac{E_{int}(\sigma)}{k_B T}\right)\right) \quad (2)$$

$$\Omega_m = \nu_D exp\left(-\frac{\Delta H_{km}(\sigma, c)}{k_B T}\right) \quad (3)$$

where ν_{dk} and ν_D are prefactors for double kink nucleation and kink migration, $\Delta H_{dk}(\sigma, c)$ is the nucleation energy barrier, $E_{int}(\sigma)$ is the solute-dislocation interaction energy which is used here to account for the solute-induced change of energy scale for kink nucleation, $\Delta H_{km}(\sigma, c)$ is the migration energy barrier which equals to zero when Si concentration is zero and increases proportionally with $\sqrt{c}|E_{int}|$. The detailed expressions for $\Delta H_{dk}(\sigma, c)$, $E_{int}(\sigma)$ and $\Delta H_{km}(\sigma, c)$ can be found in [53]. For a given combination of solute concentration c, temperature T and loading rate $\dot{\epsilon}$, the stress σ can be obtained by solving the nonlinear Eq. (1). Model parameters for Mo alloys from [53] have been recalibrated to match the experimental data for yield strength of pure Mo in the temperature range of 300 K-500 K presented in Fig. 7a. The calculated solute-dislocation interaction energy of -0.56 eV from first principle need

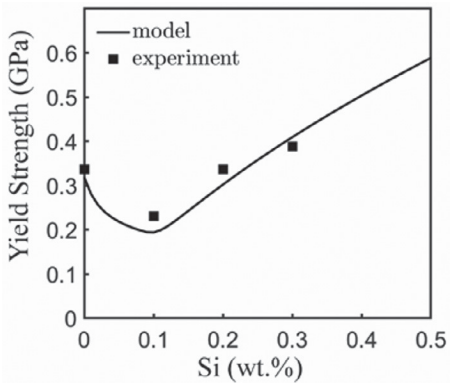

Fig. 11. Yield strength versus Si concentration for Mo-Si alloys deformed at room temperature at a constant strain rate of 5 $\times$ 10^{-4} s^{-1}. Experimental data were extracted from Fig. 7a.

be scaled as discussed in [54] because the solute-dislocation interaction in the above solid-solution model is short-ranged while in the first principle calculations, the effects of solute will extend over several lattice sites. A scaling factor of 0.8 is found to match the modeling results and the experimental data well as shown in Fig. 11 where we predict the flow stress for the Mo-Si alloys with Si concentration ranging from 0 to 0.5 wt.% deformed at room temperature and with a constant strain rate of 5 $\times$ 10^{-4}/s. The current solid-solution model could successfully capture the transition from solute softening in Mo-0.1 wt.%Si to solute hardening in Mo-0.3 wt.%Si as observed in the experiments. In other high temperature tests for the Mo-Si alloys presented in this study, thermal activation can enable the motion of the screw components, both on the primary glide plane and by cross slip. Further study is required to incorporate more deformation mechanisms into the current solid-solution model to correctly capture the higher temperature behavior of Mo-Si alloys.

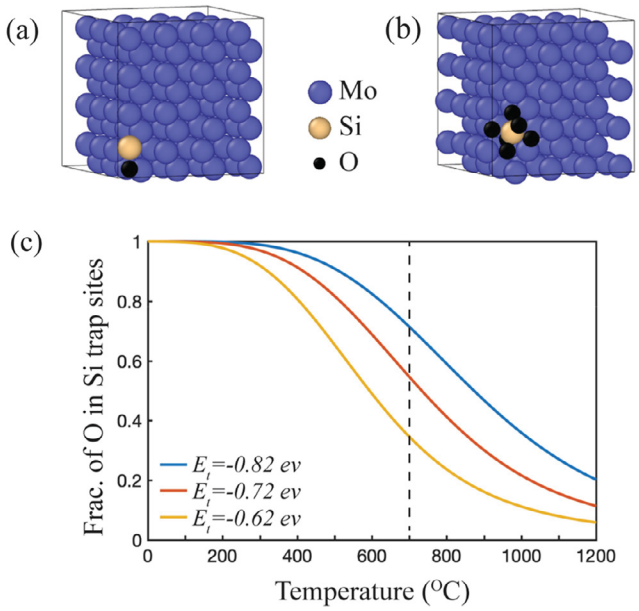

Fig. 12. Trapping of (a) one and (b) six oxygen atoms around a substitutional Si in a 128 atoms bulk BCC molybdenum supercell. **(c)** Fraction of oxygen atoms trapped around Si versus temperature in equilibrium state given different average Si-O trapping energy E_t.

5.3. Si-O interaction in the Mo-Si solid solution

Serrated flow was reported in commercial purity Mo previously in the temperature range 25°C to 500°C [55] although tests were not conducted in [55] above 500°C. An early study reported serrated flow in arc-cast Mo at temperatures as high as 700°C and 800°C [56] and claimed multiple regimes were present and attributed them to different interstitial solutes (H, C, N and O) interacting and pinning dislocations. Subsequently, Nemat-Nasser and coworkers [57] similarly claimed at least two temperature regimes in commercial purity Mo where dynamic strain aging was noted in tests conducted at a strain rate of 10^{-3} s^{-1}, and these were attributed to two different solutes (unspecified) interacting with dislocations. There is also another early report [58] that has specifically examined the role of oxygen in causing strain aging in Mo using internal friction studies. Lastly, the interaction of low levels of oxygen in tungsten (an element similar in characteristics to Mo) with screw dislocations and producing serrated flow has been studied recently by Zhao et al. [52,59].

In this study, in the Mo-0.2 wt.%Si and 0.3 wt.% Si binary alloys as well as in the ternary Mo-0.75 wt.%Si-0.14 wt.%B, serrated flow was only observed in the temperature range of 600°C-800°C and this corresponds to the high-end of the temperature range where serrated flow has been reported for commercial purity Mo. These results together with previous findings reported above prompted us to examine the role of oxygen in a Mo-Si solid solution in influencing the plastic flow response; specifically, in this section, we examine the nature of Si-O interaction in a Mo-Si solid solution to determine if insights can be gained to rationalize the shift to higher temperatures of the serrated flow behavior in Mo-Si alloys relative to commercially pure Mo.

Si (substitutional) and O (interstitial) atoms are both inserted in the bulk Mo crystal as shown in Fig. 12a, b. The inserted Si and O atoms tend to form stable bonded structure where Si has positive net atomic charge and O has negative net atomic charge. O and Si interaction energy is defined as the energy difference between the condition that O atom is close to or infinitely far away from the inserted Si atom in the Mo crystal. The first inserted O atom as shown in Fig. 12a has an interaction energy of -0.82 eV, indicating strong attraction between Si and O atoms. This strong attraction only appears to be short-range in nature and diminishes quickly to zero as the O atom moves away from the nearest interstitial sites from the Si. From the DFT calculations, we find one Si atom can effectively trap multiple O atoms, as shown in Fig. 12b where six O atoms are bound around the Si, forming a SiO_6 octahedron. This suggests possible segregation of O atoms around the Si atoms in solid solution in Mo in these Mo-Si alloys. Similar solute trapping phenomena have been studied in the context of hydrogen in steels where point and line defects, or precipitate interfaces locally trap hydrogen atoms and decrease the supply of diffusive hydrogen in the material, thereby reducing hydrogen susceptibility [60–63]. Thus, the increased temperature range for the onset of serrated flow is attributed to the trapping of O atoms by Si solute, reducing the diffusive O atoms available for DSA. As the temperature increases, O atoms separate from Si and interact with moving dislocations causing the onset of serrated flow.

With the O-Si interaction energy from DFT calculations, the equilibrium partition of O atoms between Si trap sites and Mo matrix can be derived from thermodynamic principles. The percentage of oxygen in trap sites at a given temperature is calculated as [64]:

$$\frac{n_t}{N_t - n_t} = \frac{n_l}{N_l - n_l}\exp\left(-\frac{E_t}{k_B T}\right) \tag{4}$$

where n_t and n_l are the number of solute atoms in trap sites and lattice interstitial sites in the equilibrium state, N_t and N_l are the available number of trap sites and lattice interstitial sites in the material, E_t is the interaction energy between the solute and the trap sites, k_B is the Boltzmann's constant and T is the temperature. This model considers two possible solute occupation sites, trap sites and lattice interstitial sites, ignoring the effects of other microstructural features like grain boundary, dislocations and precipitates, and it assumes the solute distribution has reached an equilibrium state. The number of available trap sites has also been assumed to be equal to the number of solutes for simplicity and is set at 0.3% in all the calculations. The model gives the change in solute partition as a function of temperature and is used to evaluate the delay in DSA due to the trapping of O atoms. The fraction of O atoms in Si trap sites at different temperatures is shown in Fig. 12c by assuming three different average solute trapping energies. These three energies are between the highest and lowest Si-O interaction energies obtained from the first-principles calculations by sequentially inserting O atoms into the interstitial sites around one Si atom. It is seen that the stable Si-O structure is strongly bound at 200°C - 300°C for all solute trapping energies used in the model and almost all the O atoms are still trapped by the Si solutes. The lack of diffusive O atoms and thus reduced oxygen-dislocation interaction rationalizes the suppression of serrated flow in Mo-Si alloys in the temperature range where DSA is observed in commercially pure Mo. As the temperature increases to 700°C and above, the Si-O complexes dissociate, and the O atoms released from the trap sites become available for interaction with moving dislocations. This agrees reasonably well with the experimentally observed 600°C temperature for the onset of serrated flow. At even higher temperatures, oxygen diffusivity would be too high to enable DSA at the strain rates in the experiments and serrated flow disappears.

Carbon is an interstitial in Mo and is also present in these alloys in levels comparable to oxygen and is expected to modify the screw dislocation core configuration in a similar manner to oxygen [51]. DFT calculations showed however that the interaction energy between Si and C is -0.71 eV while the interaction energy between Si and O as shown above is -0.82 eV. More importantly, while Si can trap six interstitial O atoms in the nearest neighbor sites as

shown in Fig. 12b, even the insertion of a second interstitial C atom around Si is found to be energetically unfavorable. These calculations show that Si induces much larger trapping effects on O atoms than it does on C atoms. Also, to fully understand the effects of C on serrated flow, we need C diffusivity data in dilute Mo-C alloys in the temperature range of interest. Unfortunately, there is no clear agreement on these data in the literature [65] to even provide a semi-quantitative assessment.

6. Discussion

6.1. Effect of Si level and temperature on yield strength and tensile elongation

The grains in the as-extruded Mo-0.2wt.%Si, Mo-0.3wt.%Si, and Mo-0.75 wt.%Si-0.14 wt.%B alloys were equiaxed (Fig. 2a,b and Fig. 3) and their dislocation densities were low (Fig. 4), indicating a recrystallized microstructure; this implies that the contribution of a high initial dislocation density on yield stress, arising from a worked structure, can be ruled out. However, the as-extruded grain size of the Mo-0.2 wt.%Si alloy (Fig. 2b) was much smaller (~10 μm) than that of the Mo-0.3 wt.%Si alloy (Fig. 2a; ~80 μm). To isolate the effect of solid solution hardening arising from a difference in Si level, the grain size contribution to yield strength needs to be removed. After the Mo-0.2 wt.%Si alloy was suitably annealed, its grain size increased to ~100 μm (Fig. 2c). Both alloys had comparable interstitial levels. Therefore, the mechanical properties of the annealed Mo-0.2 wt.%Si and the as-extruded Mo-0.3 wt.%Si alloys can be directly compared to understand the role of Si solute in affecting the mechanical response of the solid solution alloy, particularly strength, ductility, and work hardening rate. Silicon is considered a substitutional solute species in Mo, producing local elastic strains that arises from differences in atomic size and this factor is at least partially responsible for the low solubility of Si in Mo. We note here that an aspect of microstructure that was not examined but could contribute to tensile properties are differences in the distribution of grain boundary misorientations in these solid solution alloys, particularly when deformation mechanisms dependent on grain-boundary-mediated processes (for example, deformation twinning at lower temperatures or grain boundary sliding at higher temperatures) dominate. Neither of these mechanisms was observed in this study.

The variation in yield strength in uniaxial tension at room temperature (~0.1 T_m) for Mo-Si solid solution alloys with Si content is seen in Fig. 11 where a comparison of the experimental data for the commercially pure Mo, Mo-0.1 wt.%Si (from [29,55]), Mo-0.2 wt.%Si, and Mo-0.3 wt.%Si alloys with our modified solid-solution model is presented. Solid solution softening of Mo by dilute levels of substitutional solutes (Re and Pt) that was previously reported in [53] and attributed to easing double kink nucleation without hindering kink migration has been extended in this study to the flow behavior of dilute Mo-Si solid solutions.

At higher temperatures, additional deformation mechanisms that are thermally activated need to be incorporated in the model to predict flow behavior as seen in the experimental results in Fig. 7a, where the yield strength for each material (CP Mo, Mo-0.1 wt.%Si, Mo-0.2 wt.%Si, Mo-0.3 wt.%Si) is high at room temperature but then drops sharply with increasing temperature up to 300°C~500°C, beyond which it decreased more gradually with temperature. Lastly, the yield stress at ~500°C (~0.25 T_m) is significantly higher for the Mo-0.3 wt.% Si solid solution alloy compared to CP Mo, attesting to the potency of Si as a significant solid solution hardener of Mo (~ 75 MPa for CP Mo and ~ 300 MPa for the binary Mo-0.3 wt.%Si solid solution alloy).

At room temperature, increasing the Si level from 0.1 wt.% to 0.2 wt.% to 0.3 wt.% leads to a rapid decrease in ductility (Fig. 7b). In fact, ductility decreased with increasing Si level at all temperatures examined. Nevertheless, even the 0.3 wt.%Si solid solution alloy displayed ~20% ductility at 300°C (as mentioned earlier, 0.3 wt.%Si (~1 at.% Si) represents the maximum solubility of Si in Mo at 1200°C, and thus it is anticipated that at 300°C, it is somewhat lower; the equilibrium solubility of Si in Mo at 300°C is not well established) which is encouraging as it promises the ability to blunt cracks in multiphase alloys. The Mo-0.75 wt.%Si-0.14 wt.%B was brittle up to and at 400°C, implying that *significant Si supersaturation* in the Mo solid solution can be deleterious to the mechanical properties of multiphase Mo-Si-B alloys at low temperatures.

The ternary Mo-0.75 wt.%Si-0.14 wt.%B alloy displays higher yield strength, a higher tensile brittle-to-ductile transition temperature and lower ductility than the binary Mo-Si alloys in the temperature interval from 500°C to 1000°C. It is thought that B solubility in the Mo solid solution is negligible and even if present in supersaturation, is likely segregated to the grain boundaries [12,66]. Thus, the higher yield strength is thought to be a consequence of i) the finer grain size (~20 μm versus ~80-100 μm for the Mo-Si alloys), but more importantly, ii) Si supersaturation that results from the high-temperature soak at 1550°C prior to hot-extrusion that could not be subsequently relieved. EDX and EPMA analysis of the matrix solid solution phase confirmed a Si level of ~1.3-1.4 at.% and being as high as 1.7 at.%, that is higher than those in the binary alloys As mentioned previously, it is necessary to go to high temperatures, of the order of 1500°C to 1600°C for extended times (days to weeks) to relieve supersaturation but unfortunately, at these temperatures, the equilibrium solubility is of the order of ~1.5-1.8 at.% Si (Fig. 1). This higher Si level results in a strength increase and a concomitant ductility loss. Lastly, we cannot discount the fact that the low volume fraction of the coarse particles of the T_2 phase in the microstructure could aggravate the situation by providing crack nucleation sites.

6.2. Yield points, serrated flow, and yield stress and work-hardening loss with temperature

The presence of upper and lower yield points and an initial stress plateau at the lower yield point on the tensile stress-strain curves of the Mo-0.2 wt.%Si, the Mo-0.3 wt.%Si and the Mo-0.75 wt.%Si-0.14 wt.%B alloys at increasing temperatures with progressively increasing Si content implies that there is an influence of Si in solid solution on this phenomenon. Manifestation of upper and lower yield points is associated with the absence of a high initial mobile dislocation density and is related to i) the annealing step that was performed to reduce the dislocation content in the alloys prior to testing, and ii) pinning of residual dislocations by segregated solutes (O and Si) occurring during the annealing step. Our DFT calculations confirm the strong attraction of Si and O to the screw dislocation core in Mo, but while the Si does not substantially change the core structure, O modifies the screw dislocation core from an “easy-core” to a “hard-core” configuration. These observations are in accordance with a more general pattern of behavior of screw dislocations in BCC metals. For example, in bcc Fe, computations have revealed that substitutional Si is attracted to the core of the screw dislocation; once there, it influences both, kink nucleation and kink migration energies [67]. This has a profound effect on the mobility of screw dislocations, including creating a high density of jogs from cross-kink collisions and suppressing cross slip. Similarly, it has also been shown using *ab initio* calculations that interstitials (C, N, O) tend to segregate to the core of the screw dislocation in bcc Fe and transform the core from an “easy core” to a “hard core” configuration, thereby increasing the Peierls stress [51]. A strong short-range interaction was also noted in bcc W between O atoms and a screw dislocation, with an as-

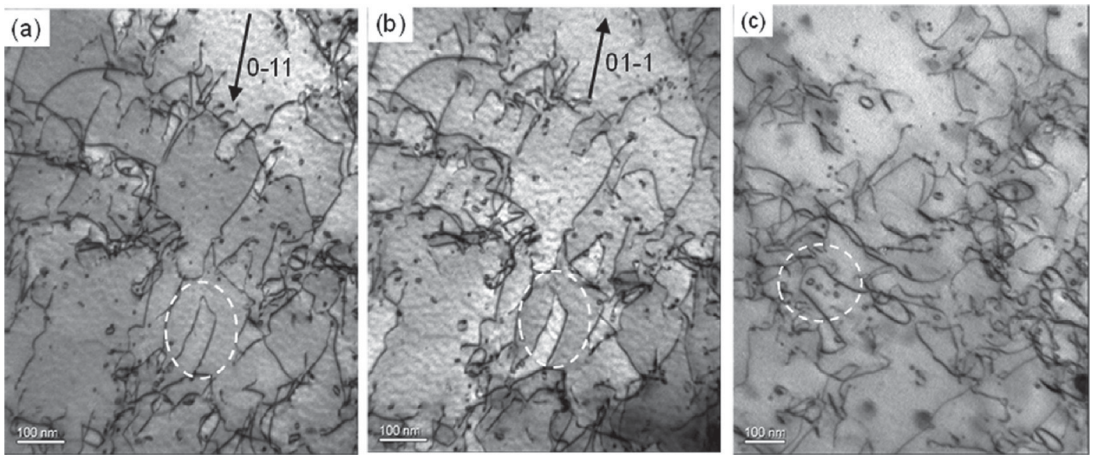

Fig. 13. Deformed microstructure in the Mo-0.75 wt.%Si-0.14 wt.%B specimens: (a,b) 800°C/10^{-4} s^{-1} and (c) 700°C/10^{-6} s^{-1}. (a,b) provide a pair of bright field TEM images satisfying the **+g/-g** condition for a one-end-closed dipole (dashed white ovals). In (c), a row of fine loops is circled using white dashed lines and may have arisen from the pinching-off of a dipole.

sociated propensity for core reconstruction from an easy core to a hard core [52,59].

Serrated flow in these solid solution alloys is a manifestation of dynamic strain aging. Serrated flow was recently reported in commercially pure Mo in the 25°C to the 500°C range [55] and early reports found serrated flow at higher temperatures as well [56,68]; its presence was argued to arise from dislocation interaction with interstitial atoms (C, N and O). In the Mo-Si and Mo-Si-B alloys examined in this study, serrated flow was only observed in the higher temperature range of 600°C-800°C. Our calculations reveal a strong short-range interaction between Si and O in the matrix, with one Si atom being able to trap six O atoms. Using the obtained interaction energy, thermodynamic calculations reveal that a significant fraction of the trapped O is released and made available to interact with dislocations in the temperature range where serrated flow is observed in these alloys.

The work-hardening behavior of bcc metals at low homologous temperatures is not as well-understood as for fcc metals. The non-planar core structure of screw dislocations in the bcc structure makes glide difficult and the motion of these straight dislocations depends on the repeated nucleation and motion of kink pairs [69,70], thus producing a thermally activated flow response in this temperature regime. However, as pointed out recently [70] in the context of work-hardening mechanisms in bcc metals, the specifics of interactions of forest dislocations with mobile dislocations need more research attention. Thus, it was shown in [71] that a mobile screw dislocation could produce a repulsive junction with a forest screw dislocation and the resulting internal stress could produce coupled motion of the pair of screw dislocations; when present in sufficient numbers, this mechanism could serve to reduce the work-hardening rate. Presumably, the apriori segregation of interstitial solute to the forest screw dislocation and modifying it to a hard core, or dynamically to the mobile screw could adversely affect this mechanism and offset the work-softening it could otherwise enable and reduce ductility.

At higher temperatures, thermally activated cross slip of screw dislocations can assist with the reduction in the work-hardening rate. Dislocation loops were observed in the specimens deformed at elevated temperatures (700°C-1000°C; Fig. 8f and Fig. 9) and were confirmed to be prismatic in character with a Burgers vector of ½[111]; such a Burgers vector (in magnitude and direction) corresponds to that for a glide dislocation in the bcc structure. In this temperature range (0.33 T_m - 0.44 T_m), the strength of these alloys gradually decreases (Fig. 7a), implying that thermally activated processes such as cross-slip and climb become increasingly active. Prismatic loops can result from the pinching-off of dipoles that are created in the structure during plastic deformation. Specifically, when a screw dislocation i) cross slips, or ii) is intersected multiple times by other dislocations moving on non-parallel planes, or iii) repeatedly intersects forest dislocations, the screw dislocation can acquire superjogs along its length. These superjogs can pin the screw dislocation and in the process, lay out edge dipoles; such edge dipoles are usually one-end-closed and an example is presented in Fig. 13a,b (highlighted using a white dashed oval) for a **+g/-g** pair obtained from a Mo-0.75 wt.%Si-0.14 wt.%B specimen deformed at 800°C/10^{-4} s^{-1}. Such edge dipoles can pinch off either due to thermally activated cross slip of the screw components (especially in bcc metals and alloys) or due to climb of the edge dislocations forming the dipole, resulting in a prismatic loop. This loop may initially be elongated but then becomes circular, or alternately, breaks into a row of smaller loops (an example is seen in Fig. 13c and was obtained from a specimen deformed at 700°C/10^{-6} s^{-1}). These dislocation configurations and how they may have evolved support the above notion of thermally activated processes gaining prominence at these temperatures and accounting for a gradual decay in yield strength.

At temperatures in excess of 1000°C, the yield strength drops off precipitously (Fig. 6d and Fig. 7a) from ~325 MPa at 1000°C and 1100°C to about 125 MPa at 1200°C for the ternary Mo-Si-B alloy and an examination of Fig. 6d shows that work softening accompanies the flow behavior from the very early stages of deformation at both 1000°C and 1200°C, clearly illustrating the influence of dynamic recovery on the flow behavior. An example of a dynamically recovered microstructure is shown in Fig. 8e for the Mo-0.3wt.%Si alloy deformed at 1000°C/5 $\times$ 10^{-4} s^{-1} and the corresponding stress-strain curve illustrating work softening is seen Fig. 5b.

7. Conclusions

We have reported on the tensile response obtained at quasi-static strain rates over a range of temperatures of three Mo-based dilute solid solution alloys, Mo-0.2 wt.%Si, Mo-0.3 wt.%Si and a ternary Mo-0.75 wt.%Si-0.14 wt.%B. The findings have been coupled with our previous results on commercially pure Mo and a binary Mo-0.1wt.% Si alloy to provide a more complete picture of the effect of Si in solid solution on yield strength, ductility, and plastic flow behavior (serrated flow). Simulations were performed to

understand (i) the influence of Si and O on the screw dislocation core structure, (ii) the origin of solid solution softening followed by hardening with increasing Si content, and (iii) the attractive Si-O interaction and how it might postpone serrated flow to higher temperatures. Deformed microstructures have been examined and dislocation configurations were characterized to rationalize the observed mechanical response.

1 A dilute level of 0.1 wt.% Si in solid solution in Mo softens it, lowering the yield strength and increasing the ductility at room temperature whereas at higher Si levels, solid solution hardening is observed. Simulations confirm this trend and the response is attributed to ease of kink nucleation transitioning to inhibiting kink migration with increasing Si content. At elevated temperatures, thermally activated processes assist dislocation activity and for all Si levels examined, only solid solution hardening is observed.
2 Although Si is attracted to the core of the screw dislocation it does not appreciably modify it; however, oxygen segregation to the core changes it from an "easy-core" to a "hard-core" configuration.
3 In the binary Mo-0.3 wt.% Si alloy, significant solid solution hardening of Mo by Si is maintained all the way up to 800°C beyond which yield strength decreases. Tensile ductility is zero at room temperature but at 300°C, it is ~20% and reaches ~35% at 400°C and 500°C;
4 Serrated flow is prominent in the 600°C-800°C regime in the three alloys examined in this study but not at lower temperatures unlike in commercial purity Mo where serrated flow is observed even at room temperature. Simulations show that this delay in the onset of serrated flow as well as the increase in serration amplitude with Si content are due to Si trapping O in the grains; in the temperature regime where serrated flow is observed, a significant fraction of the O atoms is released (detrapping) and becomes available to diffuse and pin dislocations repeatedly.
5 In the temperature regime where dynamic strain aging was observed and accompanied by significant work hardening, the deformed microstructure illustrated evidence for significant dislocation pinning and bowing with the frequent presence of dipoles and prismatic loops. The presence of one-end closed dipoles and loops suggests that these loops evolved from dipoles that have pinched off. Such dipoles evolve from superjogs pinning the movement of screw dislocations.
6 The rapid drop in strength at high temperatures ($\geq$ 1000°C) was accompanied by a significant loss in work-hardening and is attributed to dynamic recovery.
7 Lastly, it appears that if ternary Mo-rich Mo-Si-B multiphase alloys are carefully processed to restrict the Si in solid solution (i.e. avoid significant supersaturation), and if the volume fraction and distribution of the intermetallic phases are controlled, there is potential to have alloys that exhibit reasonable damage tolerance at temperatures as low as 300°C.

Declaration of Competing Interest

The authors declare that they have no known competing financial interests or personal relationships that could have appeared to influence the work reported in this paper.

Acknowledgement

The experimental work reported here was supported by the Office of Naval Research (Contract no. N00014–00-1–0373) with Dr. David Shifler as the program monitor (X.Y., P.J and SK). The simulations were supported by the National Science Foundation grant DMR-1709318 and the Extreme Science and Engineering Discovery Environment (XSEDE) grant MS090046 (Z.L. and H.G.). The authors thanks Prof. M. Heilmaier from the Karlsruhe Institute of Technology for reading the experimental parts of the manuscript and providing useful insights.

References

[1] R.C. Reed, The Superalloys, Fundamentals and Applications, Cambridge University Press, New York, 2006.
[2] J.-C. Zhao, J.H. Westbrook, Ultrahigh-temperature materials for jet engines, MRS Bull. 28 (622) (2003).
[3] R. Schafrik, R. Sprague, Superalloy technology-a perspective on critical innovations for turbine engines, Key Eng. Mater. 380 (113) (2008).
[4] D. Furrer, H. Fecht, Ni-based superalloys for turbine discs, JOM 51 (14) (1999).
[5] N.P. Padture, M. Gell, E.H. Jordan, Thermal barrier coatings for gas-turbine engine applications, Science 296 (280) (2002).
[6] J.C. Williams, E.A. Starke Jr., Progress in structural materials for aerospace systems, Acta Mater. 51 (5775) (2003).
[7] D.M. Dimiduk, J.H. Perepezko, Mo-Si-B Alloys, Developing a revolutionary turbine-engine material, MRS Bull. 28 (639) (2003).
[8] B.P. Bewlay, M.R. Jackson, J.-C. Zhao, M.G. Mendiratta, J.J. Lewandowski, P.R. Subramanian, Ultrahigh-temperature Nb-silicide-based composites, MRS Bull. 28 (646) (2003).
[9] R. Mitra, Mechanical behaviour and oxidation resistance of structural silicides, Inter. Mater. Rev. 51 (13) (2006).
[10] N.P. Padture, Advanced structural ceramics in aerospace propulsion, Nat. Mater. 15 (804) (2016).
[11] F.W. Zok, Ceramic-matrix composites enable revolutionary gains in turbine engine efficiency, Am. Ceram. Soc. Bull. 95 (22) (2016).
[12] J.H. Perepezko, R. Sakidja, K.S. Kumar, Mo-Si-B for ultra-high temperature applications, in: W.O. Soboyejo, T.S. Srivatsan (Eds.), Advanced Structural Materials: Properties, Design Optimization and Applications, 437, CRC Press, Taylor & Francis Group, 2007.
[13] M. Krüger, D. Schliephake, P. Jain, K.S. Kumar, G. Schumacher, M. Heilmaier, Effects of Zr additions on the microstructure and the mechanical behavior of PM Mo-Si-B alloys, JOM 65 (2013) 301.
[14] R. Sakidja, J.H. Perepezko, Phase stability and alloying behavior in the Mo-Si-B system, Metall. Mater. Trans. 36A (2005) 507.
[15] M. Akinc, M.K. Meyer, M.J. Kramer, A.J. Thom, J.J. Huebsch, B. Cook, Boron–doped molybdenum silicides for structural applications, Mater. Sci. Eng. A261 (1999) 16.
[16] J.H. Schneibel, R.O. Ritchie, J.J. Kruzic, P.F. Tortorelli, Optimization of Mo-Si-B intermetallic alloys, Metall. Mater. Trans 36A (2005) 525.
[17] H. Choe, J.H. Schneibel, R.O. Ritchie, On the Fracture and fatigue properties of Mo-Mo_3Si-Mo_5SiB_2 refractory intermetallic alloys at ambient to elevated temperatures (25°C to 1300°C, Metall. Mater. Trans. 34A (2003) 225.
[18] G. Hasemann, D. Kaplunenko, I. Bogomol, M. Krüger, Near-eutectic ternary Mo-Si-B alloys: microstructures and creep properties, JOM 68 (2016) 2847.
[19] K. Yoshimi, J. Nakamura, D. Kanekon, S. Yamamoto, K. Maruyama, H. Katsui, T. Goto, High-temperature compressive properties of TiC-added Mo-Si-B alloys, JOM 66 (2014) 1930.
[20] S.Y. Kamata, D. Kanekon, Y. Lu, N. Sekido, K. Maruyama, G. Eggeler, K. Yoshimi, Ultrahigh-temperature tensile creep of TiC-reinforced Mo-Si-B based alloy, Sci. Rep. 8 (2018) 10487.
[21] D. Schliephake, A. Kauffmann, X. Cong, C. Gombola, M. Azim, B. Gorr, H-J. Christ, M. Heilmaier, Constitution, oxidation and creep of eutectic and eutectoid Mo-Si-Ti alloys, Intermetallics 104 (2019) 133.
[22] S. Obert, A. Kauffmann, M. Heilmaier, Characterisation of the oxidation and creep behaviour of novel Mo-Si-Ti alloys, Acta Mater. 184 (2020) 132.
[23] A.P. Alur, N. Chollacoop, K.S. Kumar, High-temperature compression behavior of Mo-Si-B alloys, Acta Mater. 52 (2004) 5571.
[24] P. Jain, K.S. Kumar, Tensile creep of Mo–Si–B alloys, Acta Mater. 58 (2010) 2124.
[25] A.P. Alur, K.S. Kumar, Monotonic and cyclic crack growth response of a Mo-Si-B alloy, Acta Mater. 54 (2006) 385.
[26] J.H. Schneibel, High temperature strength of Mo–Mo_3Si–Mo_5SiB_2 molybdenum silicides, Intermetallics 11 (2003) 625.
[27] M. Krüger, S. Franz, H. Saage, M. Heilmaier, J.H. Schneibel, P. Jéhanno, M. Böning, H. Kestler, Mechanically alloyed Mo–Si–B alloys with a continuous α-Mo matrix and improved mechanical properties, Intermetallics 16 (2008) 933.
[28] D. Sturm, M. Heilmaier, J.H. Schneibel, P. Jéhanno, B. Skrotzki, H. Saage, The Influence of Silicon on the Strength and Fracture Toughness of Molybdenum, Mater. Sci. Eng. A463 (2007) 107.
[29] X.J. Yu, K.S. Kumar, The tensile response of Mo, Mo-Re and Mo-Si solid solutions, Int. J. Refr. Met.Hard Mater. 41 (2013) 329.
[30] L. Northcott, Molybdenum—Metallurgy of the Rarer Metals—5, Academic Press Inc., New York, 1956.
[31] M. Hansen, K. Andreko, Constitution of Binary Alloys, McGraw-Hill, New York, 1958.
[32] R. Kieffer, E. Cerwenka, Beitrag zum system molybdan-silizium, Zeits. für Metall. 43 (1952) 101.
[33] C.A. Nunes, R. Sakidja, J.H. Perepezko, Phase stability in high temperature Mo-rich Mo-B-Si alloys, in: M.V. Nathal, R. Darolia, C.T. Liu, P.L. Martin, D.B. Miracle, R. Wagner, M. Yamaguchi (Eds.), Structural Intermetallics, TMS, Warrendale, PA, 1997, p. 831.

[34] J.H. Perepezko, R. Sakidja, S. Kim, Phase stability in processing and microstructure control in high temperature Mo–Si–B alloys, in: J.H. Schneibel, K.J. Hemker, R.D. Noebe, S. Hanada, G. Sauthoff (Eds.), High Temperature Ordered Intermetallic Alloys IX, 646, Materials Research Society, Pittsburgh, PA;, 2001 N4.5.
[35] J.H. Perepezko, R. Sakidja, S. Kim, Z. Dong, J.S. Park, Multiphase microstructures and stability in high temperature Mo-Si-B alloys, in: Kevin J. Hemker, Dennis M. Dimiduk (Eds.), the Third International Symposium on Structural Intermetallics (ISSI-3), Warrendale, PA, TMS, 2002, p. 505.
[36] S. Katrych, A. Grytsiv, A. Bondar, P. Rogl, T. Velikanova, M. Bohn, Structural materials: metal–silicon–boron: on the melting behavior of Mo–Si–B alloys, J. Alloys Comp. 347 (2002) 94.
[37] P. Jain, K.S. Kumar, Dissolved Si in Mo and its effects on the properties of Mo–Si–B alloys, Scripta Mater. 62 (2010) 1.
[38] P. Van Liempt, J. Sietsma, A revised criterion for the Portevin-Le Châtelier effect based on the strain-rate sensitivity of the work-hardening rate, Metall. Mater. Trans. 42A (2011) 4008.
[39] J. Cheng, S. Nemat-Nasser, W. Guo, A unified constitutive model for strain-rate and temperature dependent behavior of Molybdenum, Mech. Mater. 33 (2001) 603.
[40] W.A. Curtin, D.L. Olmsted, L.G. Hector Jr., A predictive mechanism for dynamic strain aging in aluminium-magnesium alloys, Nature Mater. 5 (2006) 875.
[41] S.M. Keralavarma, A.F. Bower, W.A. Curtin, Quantum-to-continuum prediction of ductility loss in aluminium-magnesium alloys due to dynamic strain aging, Nat. Comm. 5 (2014) 4604, doi:10.1038/ncomms5604.
[42] P.E. Blochl, Projector augmented-wave method, Phys. Rev. B 50 (1994) 17953.
[43] G. Kresse, D. Joubert, From ultrasoft pseudopotentials to the projector augmented-wave method, Phys. Rev. B 59 (1999) 1758.
[44] J.P. Perdew, K. Burke, M. Ernzerhof, Generalized gradient approximation made simple, Phys. Rev. Lett. 77 (1996) 3865.
[45] A.N. Stroh, Dislocations and cracks in anisotropic elasticity, Philos. Mag. 3 (30) (1958) 625.
[46] J. Li, C.Z. Wang, J.P. Chang, W. Cai, V.V. Bulatov, K.M. Ho, S. Yip, Core Energy and peierls stress of a screw dislocation in bcc molybdenum: a periodic-cell tight-binding study, *Phys. Rev.* B 70 (2004) 104113.
[47] E. Clouet, L. Ventelon, F. Willaime, Dislocation core energies and core fields from first principles, Phys. Rev. Lett. 102 (2009) 055502.
[48] C. Woodward, S.I. Rao, Flexible *ab initio* boundary conditions: simulating isolated dislocations in bcc Mo and Ta, Phys. Rev. Lett. 88 (2002) 216402.
[49] A. Kumar, B.L. Eyre, Grain-boundary segregation and intergranular fracture in molybdenum, Proc. Roy. Soc. Lon. Ser.-A 370 (1743) (1980) 431.
[50] K. Leitner, P.J. Felfer, D. Holec, J. Cairney, W. Knabl, A. Lorich, H. Clemens, S. Primig, On grain boundary segregation in molybdenum materials, Mater. Des. 135 (2017) 204.
[51] B. Luthi, L. Ventelon, D. Rodney, F. Willaime, Attractive interaction between interstitial solutes and screw dislocations in bcc iron from first principles, Comp.l Mater. Sci. 148 (2018) 21.
[52] Y. Zhao, L. Dezerald, M. Pozuelo, X. Zhou, J. Marian, Simulating the mechanisms of serrated flow in interstitial alloys with atomic resolution over diffusive timescales, Nat. Comm. 11 (2020) 1227.
[53] D.R. Trinkle, C. Woodward, The chemistry of deformation: how solutes soften pure metals, Science 310 (2005) 1665 Corrections and Clarifications, Science, 311, 177(2006).
[54] Y.J. Hu, M.R. Fellinger, B.G. Bulter, Y. Wang, K.A. Darling, L.J. Kecskes, D.R. Trinkle, Z.K. Liu, Solute-induced solid-solution softening and hardening in bcc tungsten, Acta Mater. 141 (2017) 304.
[55] X.J. Yu, K.S. Kumar, Uniaxial, load-controlled cyclic deformation of recrystallized molybdenum sheet, Mater. Sci. Eng. A540 (2012) 187.
[56] G.W. Brock, Strain aging effects in arc-cast molybdenum, Trans. Metal-AIME 221 (1961) 1055.
[57] S. Nemat-Nasser, W. Guo, M. Liu, Experimentally-based micromechanical modeling of dynamic response of molybdenum, Scripta Mater. 40 (1999) 859.
[58] Y.-L. Ma, C.-Y. Sung, Strain Aging caused by oxygen in molybdenum, Acta Metall. Sinica 8 (1965) 332.
[59] Y. Zhao, L. Dezerald, J. Marian, Electronic structure calculations of oxygen atom transport energetics in the presence of screw dislocations in tungsten, Metals 9 (2019) 252.
[60] G.R. Caskey, W.L. Pillinger, Effect of trapping on hydrogen permeation, Metall. Trans. A 6 (1975) 467.
[61] G.M. Pressouyre, Trap theory of hydrogen embrittlement, Acta Metall. 28 (1980) 895.
[62] R.A. Oriani, The diffusion and trapping of hydrogen in steels, Acta Metall. 18 (1970) 147.
[63] H.K.D.H. Bhadeshia, Prevention of hydrogen embrittlement in steels, ISIJ Inter. 56 (2016) 24.
[64] I. Maroef, D.L. Olson, M. Eberhart, G.R. Edwards, Hydrogen trapping in ferritic steel weld metal, Int. Mater. Rev. 47 (2002) 191.
[65] J.-I. Imai, O. Taguchi, G.P. Tiwari, Y. Iijima, Diffusion of carbon in niobium and molybdenum, Maters. Trans., Jpn. Inst. Metals Mater. 55 (2014) 1786.
[66] F. Morito, N.I. Danylenko, H. Saito, A.V. Krajnikov, in: O.N. Senkov et al. (Eds.), Metallic Materials with High Structural Efficiency, Kluwer, Dordrecht, 2004, pp. 347–354.
[67] T. Mohri, Y. Chen, M. Kohyama, S. Ogata, A. Saengdeejing, S.K. Bhattacharya, M. Wakeda, S. Shinzato, H. Kimizuka, Mechanical properties of Fe-rich Si alloy from Hamiltonian, npj Comp. Mater. 3 (2017) 10.
[68] R.P. Carreker Jr, R.W. Guard, Tensile deformation of molybdenum as a function of temperature and strain rate, JOM, Trans. AIME 206 (1956) 178.
[69] V. Vitek, Structure of dislocation cores in metallic materials and its impact on their plastic behavior, Prog. Mater. Sci. 36 (1992) 1.
[70] M.A. Duesbery, V. Vitek, Plastic anisotropy in bcc transition metals, Acta Mater. 46 (1998) 1481.
[71] K. Srivastava, D. Weygand, D. Caillard, P. Gumbsch, Repulsion leads to coupled dislocation motion and extended work hardening in bcc metals, Nat. Comm. 11 (2020) 5098.